

# Ambient Cross-correlation Modeling for Dense Ocean-Bottom Node Arrays

Adesh Pandey, Jeffrey Shragge, and Aaron J. Girard

*Center for Wave Phenomena and Dept. of Geophysics, Colorado School of Mines, Golden CO 80401  
email: apandey@mines.edu*

## ABSTRACT

Expanding the lower-frequency bandwidth of seismic energy sources, particularly below 2.0 Hz, is crucial for the stability of full waveform inversion (FWI) analyses in seismic imaging. While traditional active sources (e.g., airguns) often struggle to effectively generate low-frequency wavefield information, the ambient seismic wavefield, generated by naturally occurring energy sources like ocean waves, offers a promising alternative that can fill this gap. However, effectively understanding and exploiting ambient wavefields requires an accurate modeling framework for simulating ambient cross-correlation wavefields. We present a methodology for accurately modeling the cross-correlation wavefield generated from ambient energy recorded on a dense ocean-bottom node (OBN) array. Our method differs from traditional ambient seismic cross-correlation modeling, which relies on Green's function (GF) retrieval assumptions including an isotropic random ambient energy source distribution and energy equipartition. The approach does not require equal energy on the causal and anticausal sides of each receiver pair to retrieve GF; rather, we treat interstation correlations as they are and directly extract information regardless of their relation to the GF, thereby obviating the need for GF retrieval assumptions. Our approach accounts for 3-D elastic seismic wave propagation within a coupled acoustic-elastic system for complex heterogeneous media. We apply the modeling method to simulate vertical-component cross correlations of ambient OBN recordings for various offshore velocity model and water depth scenarios. The analysis primarily reveals two wave types in cross-correlated data: Scholte and guided-P waves. Four key first-order control factors — energy source mechanism and location, ambient energy source distribution, earth model heterogeneity, and the bathymetric profile — all play a crucial role in the excitation and partitioning of identified wave modes. We observe that the location of ambient energy sources, whether on the seabed or at the sea surface, significantly affect the excitation, amplitude, and frequency content of the generated wave modes. Overall, understanding and exploiting the sensitivity of low-frequency ambient wavefield recorded on OBNs can open it up for subsequent long-wavelength structural imaging or elastic velocity model building for FWI analysis.

**Key words:** Seismic Interferometry, Ambient Wavefield, Green's Function, Cross-correlation Modeling

## 1 INTRODUCTION

Understanding complex Earth structure relies heavily on obtaining high-quality seismic data. While traditional acquisition strategies, primarily reliant on active-source seismic energy, have provided valuable insights, they struggle at effectively generating low-frequency (i.e., sub 2 Hz) wavefield information. However, a promising alternative source of low-frequency seismic data lies within the ambient wavefield information generated by naturally occurring energy sources like ocean waves. This ambient seis-

mic wavefield, composed mainly of surface waves such as Scholte, Love, and, under specific conditions, (leaky) Rayleigh waves, contains valuable information about subsurface properties.

Recent advances in large-scale OBN array deployments present a unique opportunity to significantly enhance our understanding of marine ambient wavefield phenomena. Ambient virtual shot gather (VSG) volumes estimated from continuous wavefield data recorded on Gulf of Mexico OBN arrays show evidence for dispersive surface- and guided P-wave modes, as well as surface-wave sensitivity to strong lateral velocity heterogeneity (e.g., salt bodies) in the sub-2.0 Hz frequency band (Girard et al., 2023). However, to fully understand and exploit the potential of the ambient OBN VSG data, it is imperative to develop a robust 3-D forward modeling framework to accurately characterize the ambient cross-correlation wavefield.

Seismic interferometry has emerged as a fundamental methodology within seismology. Seismic waves, continuously generated by a diverse array of sources ranging from oceanic phenomena to localized seismic events, serve as the basis for correlation-based interferometric analyses. Lobkis and Weaver (2001) and Wapenaar (2004) demonstrated that the interstation correlation of ambient wavefields can be approximated as the interstation GF under the assumption of diffused, equipartitioned, random, and uncorrelated “noise” field. The applicability of the interstation GF approximation to accurately imaging and estimating Earth properties, though, is limited due to the heterogeneous distribution of sources, including anthropogenic and environmental energy sources, earthquakes, and subsurface scatterers, all of which combine to prevent the ambient wavefields from achieving equipartition across the full observable seismic frequency band (Hillers et al., 2012; Liu and Ben-Zion, 2016).

Recognizing this limitation, Tromp et al. (2010) introduced a novel approach that considers both the distribution of ambient noise sources and the structural influences on interstation correlations. This approach likely is applicable for offshore exploration-scale ambient wavefield OBN recordings characterized by an acoustic-elastic coupled seabed, significant bathymetric variations, and varying ambient energy sources with respect to location, distribution and directivity. However, before applying this approach for imaging and inversion activities, we first need to assess its applicability in modeling the cross-correlation wavefield for OBN VSG data and better understand the underlying differences from the interstation GF modeling approach.

This paper begins with restating the theoretical foundation of Tromp et al. (2010) with a minor adjustments to allow the modeling of cross-correlation wavefields recorded on dense OBNs. Next, we compare the results of the cross-correlation modeling (CCM) approach with those obtained by the GF retrieval approach. We then use the outlined modeling method to simulate the interferometric wavefield for different synthetic offshore velocity model scenarios, ambient energy source locations, and ocean bathymetry to understand the excitation and behaviour of surface- and body-wave modes. We conclude by outlining other key control factors currently under investigation, the interplay of which influences wave-mode excitation and energy partitioning.

## 2 METHOD

### 2.1 Modeling ambient cross-correlation functions

Choosing not to rely on GF retrieval assumptions and instead interpreting cross-correlation functions (CCFs) as self-consistent observables represents a departure from established methods. Thus, we present a comprehensive derivation of the time-domain equations for modeling CCFs between receiver pairs. This CCF modeling methodology is derived from the work of Tromp et al. (2010). We refer this approach herein as cross-correlation modelling (CCM).

The continuous CCF, denoted  $\mathcal{C}_{ij}$ , of two ambient wavefield recordings  $v_i$  and  $v_j$  at receiver locations  $\mathbf{x}_1 = (x_1, y_1, z_1)$  and  $\mathbf{x}_2 = (x_2, y_2, z_2)$ , respectively, of duration of  $T$ , is explicitly given by:

$$\mathcal{C}_{ij}(\mathbf{x}_1, \mathbf{x}_2, \tau) = \int_{-T/2}^{T/2} v_i(\mathbf{x}_1, t) \cdot v_j(\mathbf{x}_2, t + \tau) dt = [v_i(\mathbf{x}_1, -t) * v_j(\mathbf{x}_2, t)](\tau), \quad (1)$$

where  $t$  denotes time;  $\tau$  is the temporal cross-correlation lag; and  $v_i$  and  $v_j$  are the  $i$  and  $j$  components of the ground velocity vector recorded at the two receivers  $\mathbf{x}_1$  and  $\mathbf{x}_2$ , respectively.

Wavefield  $v_i(\mathbf{x}, t)$  excited by the ambient wavefield sources  $N$  and recorded at  $\mathbf{x}$  can be expressed through the velocity Green’s function  $G_{in}$  (Aki and Richards, 2002) as

$$v_i(\mathbf{x}, t) = \int_{\partial D} [G_{in}(\mathbf{x}, \boldsymbol{\xi}, t') * N_n(\boldsymbol{\xi}, t')](t) d\boldsymbol{\xi}, \quad (2)$$

where  $G_{in}(\mathbf{x}, \boldsymbol{\xi}, t')$  represents the  $i$  component of particle velocity at  $\mathbf{x}$  due to a impulsive source in the  $n$  direction at  $\boldsymbol{\xi}$ ;  $N_n(\boldsymbol{\xi}, t')$  denotes the  $n$ th component of the ambient energy source field as a function of location  $\boldsymbol{\xi}$  and time  $t'$ ; and  $\partial D$  is the domain boundary. Convolution of wavefields  $v_i(\mathbf{x}_1, -t)$  with  $v_j(\mathbf{x}_2, t)$  results in the time-domain CCF

$$\mathcal{C}_{ij}(\mathbf{x}_1, \mathbf{x}_2, \tau) = [v_i(\mathbf{x}_1, -t) * v_j(\mathbf{x}_2, t)](\tau), \quad (3)$$

$$= \int \int_{\partial D} [[G_{in}(\mathbf{x}_1, \boldsymbol{\xi}_1) * N_n(\boldsymbol{\xi}_1)](-t) * [G_{jm}(\mathbf{x}_2, \boldsymbol{\xi}_2) * N_m(\boldsymbol{\xi}_2)](t)](\tau) d\boldsymbol{\xi}_1 d\boldsymbol{\xi}_2. \quad (4)$$

Rearranging the convolution leads to

$$\mathcal{C}_{ij}(\mathbf{x}_1, \mathbf{x}_2, \tau) = \int \int_{\partial D} [G_{jm}(\mathbf{x}_2, \boldsymbol{\xi}_2, t) * G_{in}(\mathbf{x}_1, \boldsymbol{\xi}_1, -t)] * [N_n(\boldsymbol{\xi}_1, -t) * N_m(\boldsymbol{\xi}_2, t)](\tau) d\boldsymbol{\xi}_1 d\boldsymbol{\xi}_2. \quad (5)$$

Usually, large numbers of windowed cross-correlations of continuous ambient wavefield recordings are stacked to enhance coherent signals and downweight incoherent noise. Therefore, we take the ensemble CCF given by

$$\langle \mathcal{C}_{ij}(\mathbf{x}_1, \mathbf{x}_2, \tau) \rangle = \int \int_{\partial D} [G_{jm}(\mathbf{x}_2, \boldsymbol{\xi}_2, t) * G_{in}(\mathbf{x}_1, \boldsymbol{\xi}_1, -t)] * \langle [N_n(\boldsymbol{\xi}_1, -t) * N_m(\boldsymbol{\xi}_2, t)] \rangle(\tau) d\boldsymbol{\xi}_1 d\boldsymbol{\xi}_2, \quad (6)$$

where  $\langle \cdot \rangle$  denotes an ensemble average. Following the common assumption that “noise” is “spatially uncorrelated” over distances much smaller than the seismic wavelength (Wapenaar, 2004; Wapenaar and Fokkema, 2006), we express the ensemble average of the ambient wavefield sources with a spatial delta function  $\delta$  and a source autocorrelation  $S_{nm}(t)$  given as

$$\langle N_n(\boldsymbol{\xi}_1, -t) * N_m(\boldsymbol{\xi}_2, t) \rangle = S_{nm}(\boldsymbol{\xi}_1, t) \cdot \delta(\boldsymbol{\xi}_1 - \boldsymbol{\xi}_2), \quad (7)$$

which simplifies the ensemble CCF to

$$\langle \mathcal{C}_{ij}(\mathbf{x}_1, \mathbf{x}_2, \tau) \rangle = \int_{\partial D} G_{jm}(\mathbf{x}_2, \boldsymbol{\xi}, t) * [G_{in}(\mathbf{x}_1, \boldsymbol{\xi}, -t) * S_{nm}(\boldsymbol{\xi}, t)](\tau) d\boldsymbol{\xi}. \quad (8)$$

Using source-receiver reciprocity, we can rewrite the ensemble CCF as

$$\langle \mathcal{C}_{ij}(\mathbf{x}_1, \mathbf{x}_2, \tau) \rangle = \int_{\partial D} G_{jm}(\mathbf{x}_2, \boldsymbol{\xi}, t) * [G_{ni}(\boldsymbol{\xi}, \mathbf{x}_1, -t) * S_{nm}(\boldsymbol{\xi}, t)](\tau) d\boldsymbol{\xi}. \quad (9)$$

For a narrow frequency band (e.g., 0.05-1.0 Hz), the ambient energy source function  $S_{nm}$  can be partitioned into its spatial and temporal dependencies as

$$S_{nm}(\boldsymbol{\xi}, t) = S_{nm}(\boldsymbol{\xi}) \cdot S(t), \quad (10)$$

where (1) the relative spatial distribution of ambient wavefield energy is defined such that  $S_{nm}(\boldsymbol{\xi}) = 0$  and  $S_{nm}(\boldsymbol{\xi}) = 1$  represent effective sources with zero and the highest energy at location  $\boldsymbol{\xi}$ , respectively; and (2)  $S(t)$  is the ambient wavefield source-time autocorrelation function. With these definitions, the CCF becomes

$$\langle \mathcal{C}_{ij}(\mathbf{x}_1, \mathbf{x}_2, \tau) \rangle = \int_{\partial D} G_{jm}(\mathbf{x}_2, \boldsymbol{\xi}, t) * [G_{ni}(\boldsymbol{\xi}, \mathbf{x}_1, -t) * (S_{nm}(\boldsymbol{\xi}) \cdot S(t))](\tau) d\boldsymbol{\xi}, \quad (11)$$

or

$$\langle \mathcal{C}_{ij}(\mathbf{x}_1, \mathbf{x}_2, \tau) \rangle = \int_{\partial D} G_{jm}(\mathbf{x}_2, \boldsymbol{\xi}, t) * [(G_{ni}(\boldsymbol{\xi}, \mathbf{x}_1, -t) \cdot S_{nm}(\boldsymbol{\xi})) * S(t)](\tau) d\boldsymbol{\xi}. \quad (12)$$

From this equation, we can now define the driving source of the ensemble CCF  $\langle \mathcal{C}_{ij} \rangle$  as

$$f_m(\boldsymbol{\xi}, \mathbf{x}_1, t) = (G_{ni}(\boldsymbol{\xi}, \mathbf{x}_1, -t) \cdot S_{nm}(\boldsymbol{\xi})) * S(t), \quad (13)$$

which is simply the noise source-energy weighted time-reversed wavefield recorded at noise locations  $\boldsymbol{\xi}$  due to a source with source-time function  $S(t)$  at the virtual shot point locations  $\mathbf{x}_1$ .

Ocean-wave-generated ambient wavefields (Hasselmann, 1963; Arduin and Herbers, 2013; Arduin et al., 2015) can be approximated by the combination of tangential stress and vertical pressure force acting at the sea surface and on the local bathymetry (Nakata et al., 2019). We assume that these ambient wavefield sources are sufficient to explain the ambient wavefield OBN recordings. Therefore, the ensemble CCF for ambient OBN recordings can be written as

$$\langle C_{ij}(\mathbf{x}_1, \mathbf{x}_2, \tau) \rangle = \int_{\partial D} G_{jp}(\mathbf{x}_2, \boldsymbol{\xi}, t) * [(G_{pi}(\boldsymbol{\xi}, \mathbf{x}_1, -t) \cdot S(\boldsymbol{\xi})) * S(t)](\tau) d\boldsymbol{\xi}, \quad (14)$$

where  $S(t)$  is the pressure-source autocorrelation function; and subscript  $p$  denotes the pressure component.

## 2.2 CCF forward modeling workflow

Equation 14 can be used to model CCFs for dense OBN arrays without necessitating a GF approximation. We model a virtual shot gather (VSG) for a virtual shot point located at  $\mathbf{x}_1$  using a numerically coupled acoustic-elastic wave propagation solver by performing the following steps:

- (1) Characterize the spatial distribution of ensemble-averaged ambient wavefield energy  $S(\boldsymbol{\xi})$ .
- (2) For  $i = x-, y-,$  or  $z-$ velocity component, inject a force source in the  $i$ th direction at the virtual shot point location  $\mathbf{x}_1$ . For  $i = p$ , inject an explosive source ( $\sigma_{xx} = \sigma_{yy} = \sigma_{zz}$ ). In either case, the source-time function  $S(t)$  has a frequency spectrum of the ensemble-averaged ambient wavefield energy.
- (3) Record the pressure-component wavefield at locations  $\boldsymbol{\xi}$  due to the source implemented in Step 2.
- (4) Time reverse the recorded pressure-component wavefield and multiply it by ensemble-averaged ambient wavefield energy  $S(\boldsymbol{\xi})$  to generate the driving source  $f_p$  (equation 8) needed to model the ensemble CCFs (equation 7).
- (5) Inject explosive sources at ambient wavefield locations  $\boldsymbol{\xi}$  with source-time function as  $f_p$  and sample the wavefield components (i.e., particle velocity  $x, y, z$  and pressure  $p$ ) at other OBN locations  $\mathbf{x}_2$  to compute the desired VSG.

If, in Step 2,  $i = z$ , i.e., a vertical force source is injected, then for the sampled wavefield  $z$ -component in Step 5, the modeled CCFs would be a  $C_{zz}$  VSG. Similarly, for  $i = x$ , i.e., a horizontal force source is injected in Step 2, and the  $y$ -wavefield component is sampled in Step 5, the CCFs would be the cross-component  $C_{xy}$  VSG.

## 2.3 Green's function modeling

Under GF retrieval using seismic interferometry assumptions including energy equipartition and diffused field (Lobkis and Weaver, 2001; Sánchez-Sesma and Campillo, 2006; Weaver and Lobkis, 2004), isotropic distribution of spatially uncorrelated noise sources (Wapenaar, 2004; Wapenaar and Fokkema, 2006), equation 8 can be written as (see Wapenaar and Fokkema (2006); Wapenaar et al. (2010a,b) for GF retrieval using seismic interferometry derivations),

$$\langle C_{ij}(\mathbf{x}_1, \mathbf{x}_2, \tau) \rangle \approx [G_{ji}(\mathbf{x}_2, \mathbf{x}_1, t) + G_{ji}(\mathbf{x}_2, \mathbf{x}_1, -t)] * S(t). \quad (15)$$

Equation 15 shows that under Green's function retrieval assumptions, the CCF can be obtained as interstation Green's function between  $\mathbf{x}_1$  and  $\mathbf{x}_2$  plus its time-reversed version, convolved with  $S(t)$ , the autocorrelation of the ambient wavefield energy source-time function. We refer this modeling approach as Green's function modeling (GFM) in this paper.

## 2.4 Comparison of CCF and GF modeling approaches

We first compare the GFM and CCM forward modeling approaches using a flat ocean-bottom model with a 1.5 km water depth. The ocean-bottom velocities are set at  $v_p = 1.8$  km/s and  $v_s = 0.6$  km/s respectively, with  $v_p$  and  $v_s$  gradients of 0.43 km/s per km for and 0.27 km/s per km, respectively. The region of interest extends 190 km  $\times$  190 km  $\times$  15 km ( $x \times y \times z$ ) with the virtual shot point at  $[x_0, y_0, z_0] = [95.0, 95.0, 1.49]$  km. For convenience, we show only the positive lag times and positive offsets with respect to the virtual shot point. We use an Ormsby wavelet with a flat frequency spectrum between 0.05 Hz to 0.8 Hz as the ambient wavefield energy source-time autocorrelation function for all modeling results presented in this paper.

Figure 1a and 1b show the Z-component VSG and corresponding phase-velocity-frequency (PVF) plot simulated using GFM approach. Two distinct wave modes are observed in the VSG: the dominant Scholte ( $S_c$ ) waves indicated by white arrows, and the weaker guided-P waves at locations indicated by yellow arrows. The fundamental Scholte wave mode  $S_c^0$  exhibits higher energy compared to the higher-order Scholte wave modes. From the PVF plot, one can clearly identify weaker guided-P waves and at least three branches of higher-order Scholte wave modes ( $S_c^1, S_c^2, S_c^3$ ).

Figure 1c and 1d present the Z-component VSG and corresponding PVF plot modeled using CCM approach for ambient wavefield energy sources uniformly distributed at the ocean bottom. The VSG images appear to exhibit a filtering effect on the

Case	P-wave velocity $v_p$ (m/s)	S-wave velocity $v_s$ (m/s)	Density $\rho(\text{kg/m}^3)$
SB	1700	600	2100
HB	3500	1700	2100

**Table 1.** Soft ocean-bottom (SB) and hard ocean-bottom (HB) velocity model parameters.

lower-energy, higher-order  $S_c$  and guided P-wave modes, as they are relatively weak as compared to those in the VSG presented in Figure 1a. The guided-P wave appears completely absent too.

In contrast, Figures 1e and 1f illustrate the Z-component VSG and PVF plot using the CCM approach with ambient wavefield energy sources uniformly distributed at the ocean surface. The fundamental  $S_c^0$  wave mode exhibits a lower frequency range ( $\sim 0.2$ - $0.35$  Hz), while the guided-P waves are notably stronger compared to the scenario where ambient energy sources are located at the ocean bottom (Figure 1c or when VSG is modeled using GFM approach (Figure 1a)).

The noted differences in wave signatures highlight the potential impact of choosing the GFM or CCF modeling approaches when using ambient forward modeling for imaging or inversion applications. Clearly, the two modeling approaches produce different wave signatures. By disregarding the underlying GF assumptions, the CCFs do not approximate the interstation GFs. This is particularly evident when the ambient wavefield energy sources act at the ocean surface. Recognizing that the GF retrieval assumptions are difficult to satisfy for low-frequency (sub-1.0 Hz) OBN ambient wavefield recording, we opt to use the CCM approach to model CCFs in the results presented below.

### 3 SYNTHETIC EXPERIMENTS

In this section, we simulate the Z-component cross-correlation wavefield recorded on OBNs using CCM approach for different GOM velocity model scenarios using a 3-D spectral element method (SEM; Komatitsch et al. (2000)). The synthetic model is  $190 \text{ km} \times 190 \text{ km} \times 15 \text{ km}$  ( $x \times y \times z$ ) with a regular grid spacing of  $0.6 \text{ km} \times 0.6 \text{ km} \times 0.25 \text{ km}$  ( $dx \times dy \times dz$ ). We begin with a flat seafloor and 1-D  $v_p(z)$  and  $v_s(z)$  velocity profiles beneath the ocean bottom. To study the different wave-modes in the modeled cross-correlation wavefields and their dispersion characteristics, we use two groups of ocean-bottom velocity models: (1) soft bottom (SB) with the  $v_s$  at the ocean bottom being much slower than the acoustic fluid velocity; and (2) hard bottom (HB) with  $v_s$  at the ocean bottom faster than the acoustic fluid velocity. Table 1 presents the properties of the ocean-bottom models. Each model also has approximate GOM  $v_p$  and  $v_s$  gradients of  $0.43 \text{ km/s per km}$  and  $0.27 \text{ km/s per km}$ , respectively.

#### 3.1 Uniform noise source distribution at different depths in ocean water layer

At frequencies below  $<1$  Hz, the observed ambient wavefield energy is primarily generated by ocean waves driven by two main mechanisms: interference of ocean waves with bottom topography (primary mechanism) and interference of pairs of ocean wave trains (secondary mechanism) (Longuet-Higgins, 1950; Hasselmann, 1963; Arduin and Herbers, 2013). In the primary mechanism, the seismic source can be described as a combination of a tangential stress and a vertical pressure force acting on the local bathymetry while in the secondary mechanism, the source is a distributed pressure field on the ocean surface (Nakata et al., 2019).

To investigate the excitation of different wave modes and their characteristics due to the location of ambient wavefield energy sources, we uniformly distributed ambient energy at various depths within the ocean water layer. The ocean-bottom depth was kept constant at  $1.5 \text{ km}$ , and the OBNs were positioned just below the ocean bottom at  $1.51 \text{ km}$ . Figures 2 and 3 depict the VSGs (left column) and corresponding PVF plots (right column) for the SB and HB model scenarios, respectively, with ambient energy sources at: (a-b) the surface, (c-d)  $0.5 \text{ km}$  depth, (e-f)  $0.75 \text{ km}$  depth, (g-h)  $1.0 \text{ km}$  depth, and (i-j)  $1.5 \text{ km}$  at the seabed.

From both the SB and HB cases in Figures 2 and 3, respectively, we observe that the ambient energy sources at and close to the ocean surface (Figure 2a and 3a) generate the strongest guided P-wave amplitudes (yellow arrows). The number of observed guided P-wave modes in the VSG decreases as the ambient energy sources approach the seabed (Figure 2i and 3i). Guided-P waves are nearly absent in the VSGs and corresponding PVFs when the ambient energy sources are close to the seabed. The PVF plots exhibit a clear truncation effect when the guided P-wave modes are present: the high-frequency band and high-mode dispersion energy of the Scholte wave modes (white arrows), are suppressed by the strong dispersive guided P-wave modes. The Scholte wave truncation frequency corresponds to the low cutoff frequency of the guided P-wave mode (i.e., the white vertical lines in Figures 2a).

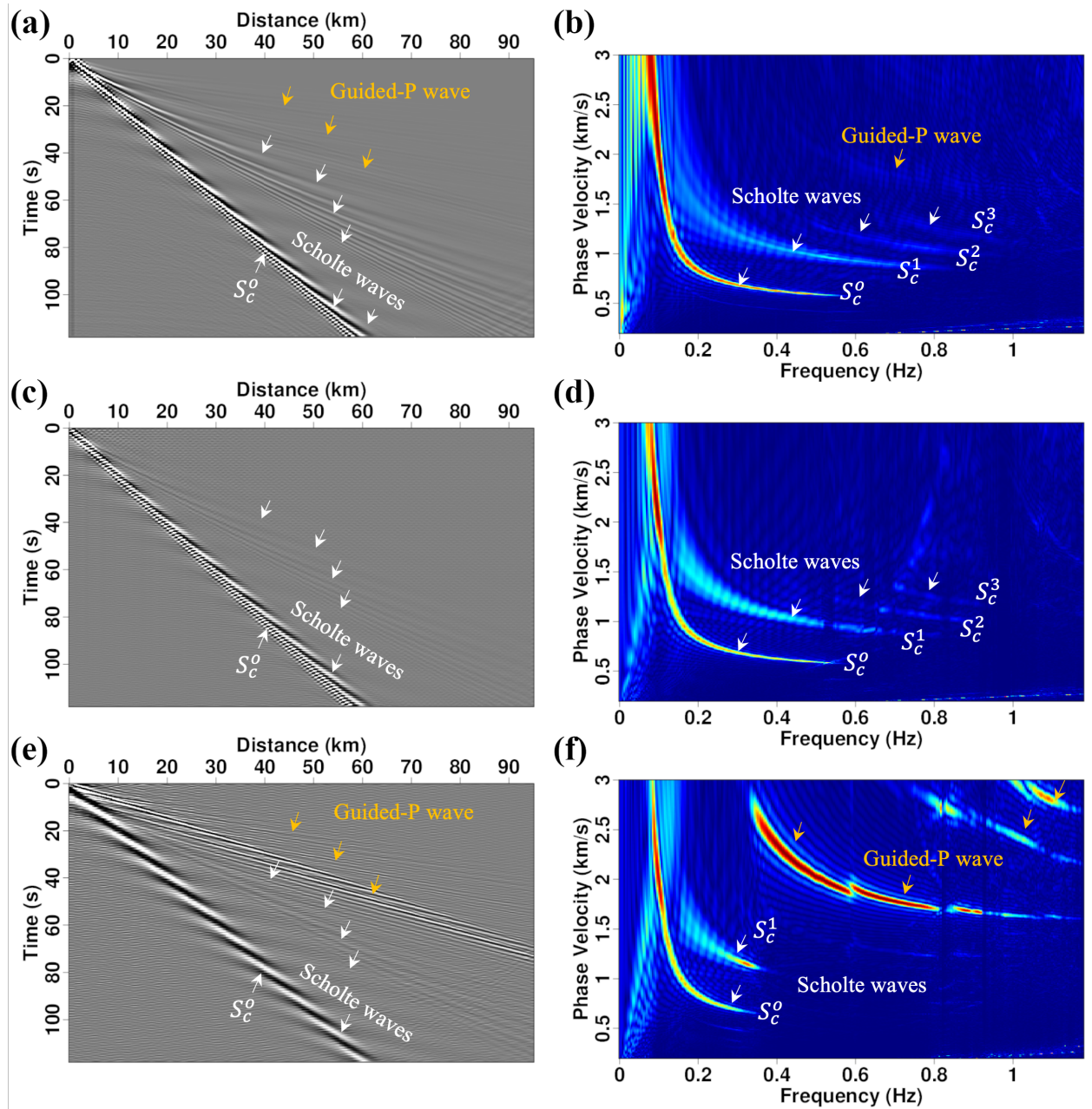


**Figure 1.** Comparison of modeled VSGs (left column) and corresponding PVF panel (right column) obtained using GFM and CCM approaches. The white and yellow arrows indicate Scholte and guided P-wave modes, respectively. (a) VSG and (b) the associated PVF plot using the GFM approach. (c) VSG and corresponding (d) PVF plot using the CCM approach for noise sources at the ocean bottom. (e) VSG and the associated (f) PVF plot using the CCM approach for ambient energy sources acting at the ocean surface.

### 3.2 Effect of ocean-water depth on Scholte and guided P-wave excitation

We consider a SB model with three constant ocean water depths: (1) 0.5 km, (2) 1.5 km, and (3) 3.0 km. The OBNs are positioned 10 m below the ocean floor and the ambient energy sources are uniformly distributed over the surface. Figure 4 presents the Z-component VSG and associated PVF plots to illustrate the effects of water depth on the partitioning of Scholte and guided P-wave energy. We observe that the guided P-wave energy (yellow arrows) becomes dominant with increasing water depth, resulting in the

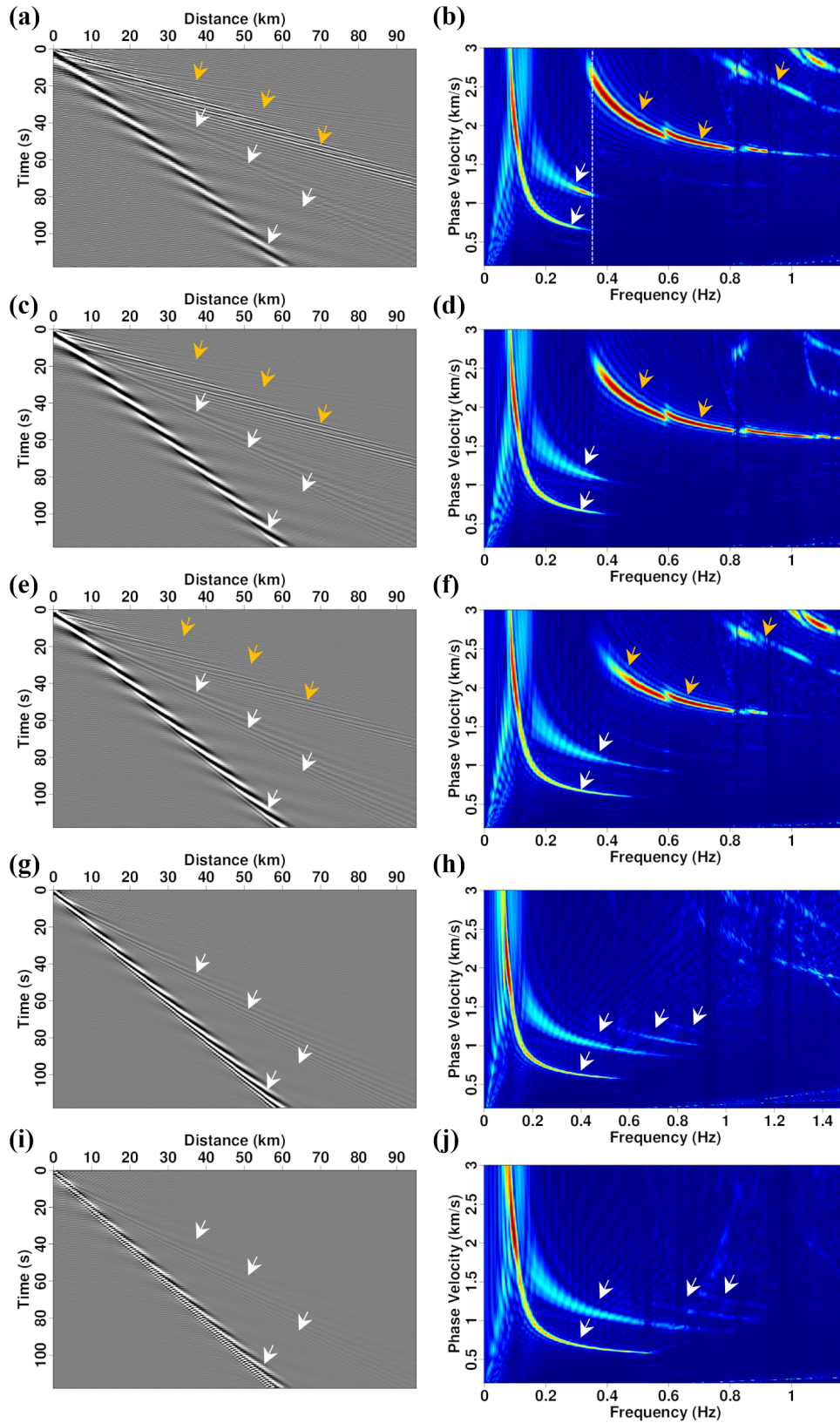


**Figure 2.** CCM VSGs (left column) alongside their corresponding PVF panel (right column) for the SB model with a constant 1.5 km water depth. Scholte and guided P-wave modes are highlighted by white and yellow arrows, respectively. The ambient energy sources are uniformly distributed at the following depths: (a-b) 0.01 km, (c-d) 0.5 km, (e-f) 0.75 km, (g-h) 1.0 km, and (i-j) 1.5 km.

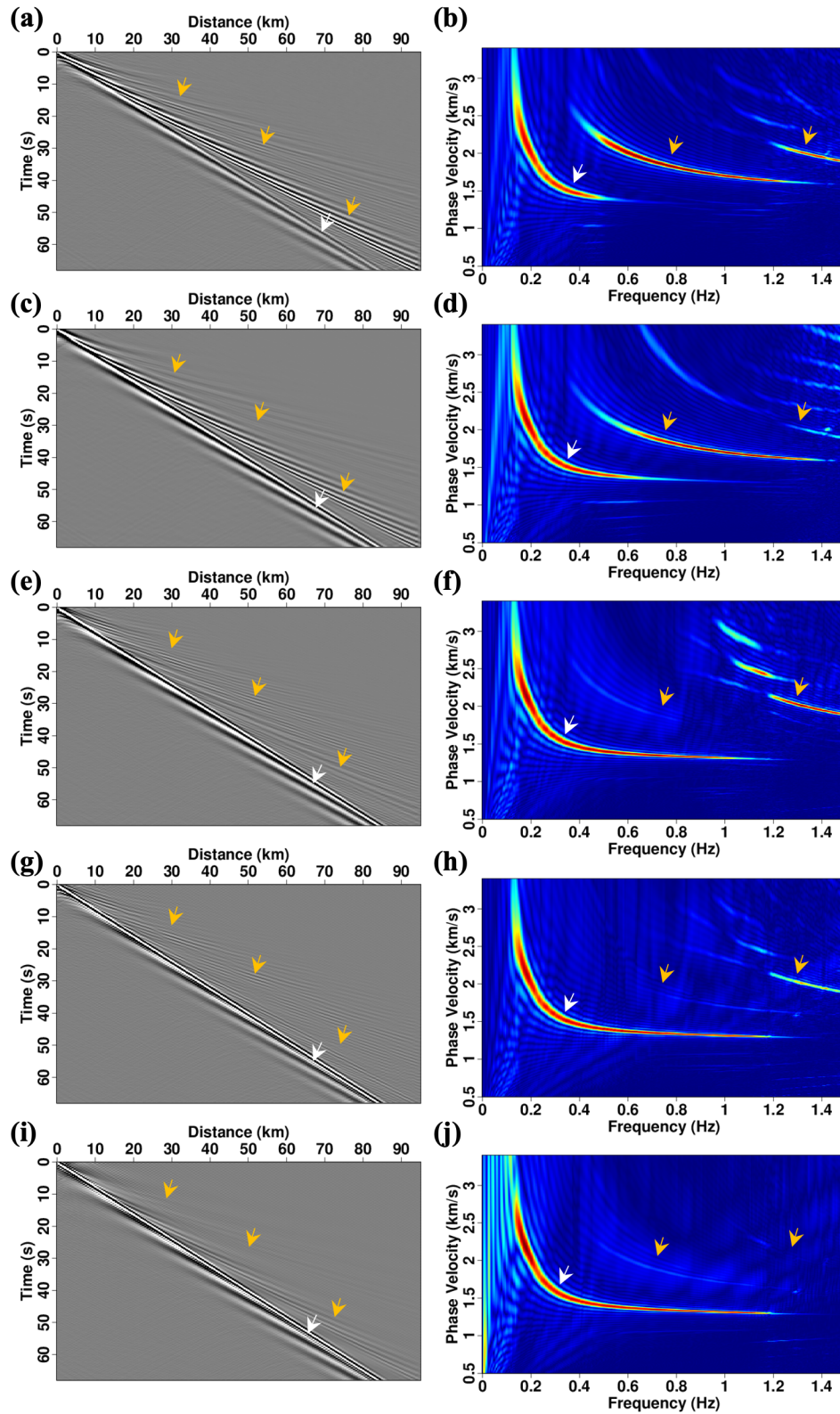


**Figure 3.** CCM VSGs (left column) alongside their corresponding PVF panel (right column) for the HB model with a constant 1.5 km water depth. Scholte and guided P-wave modes are highlighted by white and yellow arrows, respectively. The ambient energy sources are uniformly distributed at the following depths: (a-b) 0.01 km, (c-d) 0.5 km, (e-f) 0.75 km, (g-h) 1.0 km, and (i-j) 1.5 km

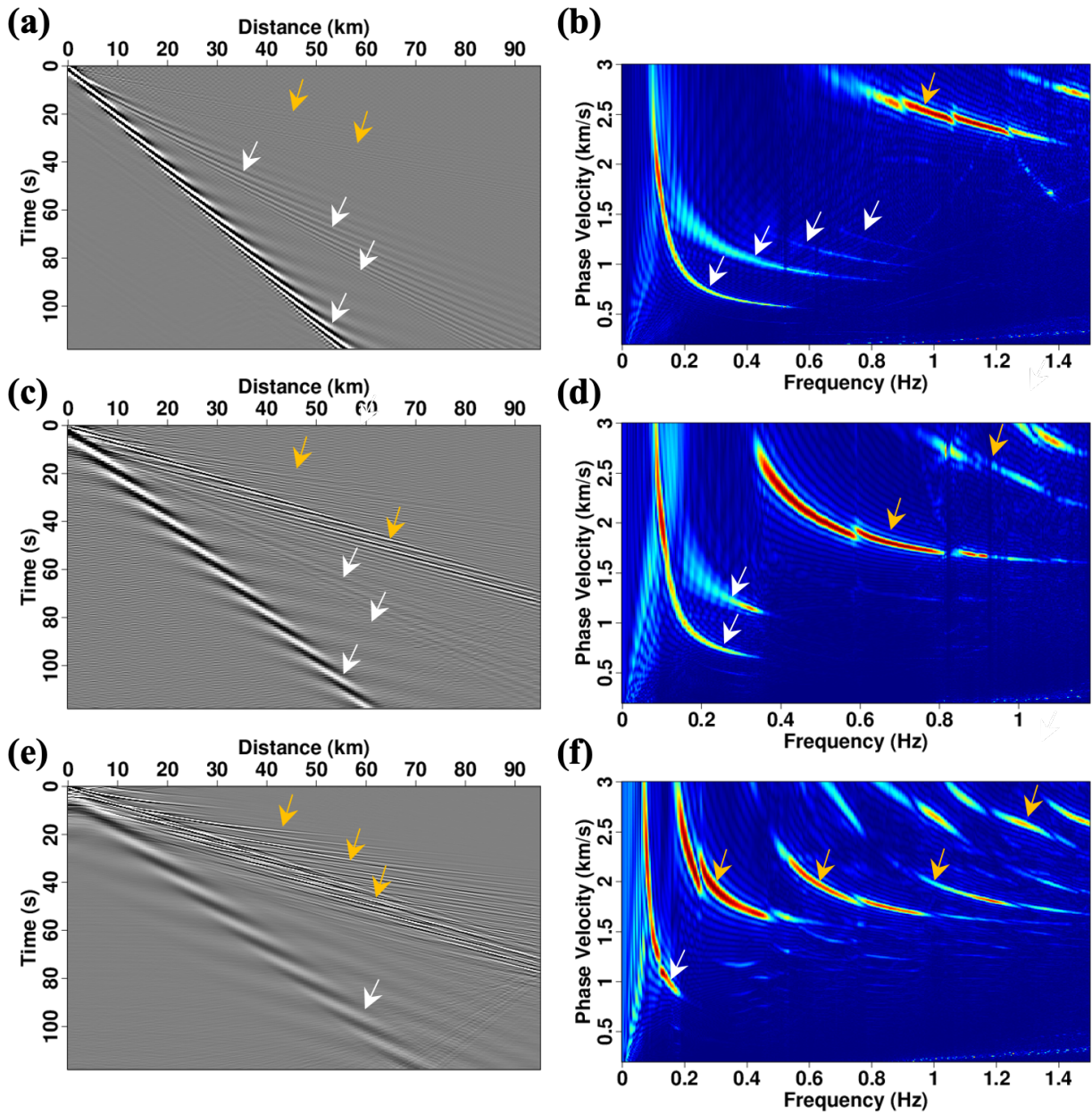


**Figure 4.** CCM VSGs (left column) with the corresponding PVF panel (right column) for the SB model with water depths of: (a-b) 0.5 km, (c-d) 1.0 km, and (e-f) 1.5 km. Scholte and guided P-wave modes are highlighted by white and yellow arrows, respectively.

truncation of the high-frequency band and higher modes of Scholte waves (white arrows) and, hence, leading to a narrower Scholte frequency band.

#### 4 CONCLUSIONS AND FUTURE WORK

We present a cross-correlation modeling (CCM) methodology for ambient seismic cross-correlation wavefields recorded on dense ocean bottom node (OBN) arrays. The CCM approach diverges from traditional ambient wavefield modeling reliant on Green's function retrieval assumptions, and offers a more flexible and accurate modeling framework. By applying this method to model

vertical cross-correlations for various offshore velocity models and water-depth scenarios, we identify two primary wave types: Scholte and guided-P waves. Synthetic experiments revealed distinct differences in wave signatures resulting from different ambient energy source locations and ocean water depths. Notably, the presence and dominance of guided P-wave modes are observed to increase with greater water depths, affecting the energy distribution and frequency content of the Scholte waves. While our current research focuses on modeling the cross-correlation wavefield and investigating the ambient energy source mechanism and location, ongoing and future work is dedicated to investigating other key control factors - noise source distribution, velocity heterogeneity, and bathymetric profile - that influence the excitation and partitioning of surface-, body-, and guided P-wave modes. By further understanding these factors, we aim to enhance our ability to accurately model and interpret ambient seismic cross-correlations for OBNs, ultimately enabling us to accurately model and invert the low-frequency ambient data recorded on OBNs in Gulf of Mexico for low-frequency elastic velocity model building.

## 5 ACKNOWLEDGEMENTS

We thank the sponsor companies of the Center for Wave Phenomena, whose support made this research possible. The reproducible numerical examples presented in this paper were run on Mines Wendian High-Performance-Computing platform using open-source SpecFEM3D software package as the forward modeling engine.

## REFERENCES

- Aki, K., and P. Richards, 2002, *Quantitative seismology*, 2nd edition: University Science Books, Sausalito, CA.
- Ardhuin, F., L. Gualtieri, and E. Stutzmann, 2015, How ocean waves rock the earth: Two mechanisms explain microseisms with periods 3 to 300 s: *Geophysical Research Letters*, **42**, 765–772.
- Ardhuin, F., and T. H. Herbers, 2013, Noise generation in the solid earth, oceans and atmosphere, from nonlinear interacting surface gravity waves in finite depth: *Journal of Fluid Mechanics*, **716**, 316–348.
- Girard, A. J., J. Shragge, and B. Olofsson, 2023, Low-frequency ambient ocean-bottom node surface-wave seismology: A Gulf of Mexico case history: *Geophysics*, **88**, B21–B32.
- Hasselmann, K., 1963, A statistical analysis of the generation of microseisms: *Reviews of Geophysics*, **1**, 177–210.
- Hillers, G., M. Campillo, Y.-Y. Lin, K.-F. Ma, and P. Roux, 2012, Anatomy of the high-frequency ambient seismic wave field at the TCDP borehole: *Journal of Geophysical Research: Solid Earth*, **117**.
- Komatitsch, D., C. Barnes, and J. Tromp, 2000, Wave propagation near a fluid-solid interface: A spectral-element approach: *Geophysics*, **65**, no. 2, 623–631.
- Liu, X., and Y. Ben-Zion, 2016, Estimating correlations of neighbouring frequencies in ambient seismic noise: *Geophysical Journal International*, **206**, 1065–1075.
- Lobkis, O. I., and R. L. Weaver, 2001, On the emergence of the Green’s function in the correlations of a diffuse field: *The Journal of the Acoustical Society of America*, **110**, 3011–3017.
- Longuet-Higgins, M. S., 1950, A theory of the origin of microseisms: *Philosophical Transactions of the Royal Society of London. Series A, Mathematical and Physical Sciences*, **243**, 1–35.
- Nakata, N., L. Gualtieri, and A. Fichtner, 2019, *Seismic ambient noise*: Cambridge University Press.
- Sánchez-Sesma, F. J., and M. Campillo, 2006, Retrieval of the Green’s function from cross correlation: the canonical elastic problem: *Bulletin of the Seismological Society of America*, **96**, 1182–1191.
- Tromp, J., Y. Luo, S. Hanasoge, and D. Peter, 2010, Noise cross-correlation sensitivity kernels: *Geophysical Journal International*, **183**, 791–819.
- Wapenaar, K., 2004, Retrieving the elastodynamic Green’s function of an arbitrary inhomogeneous medium by cross correlation: *Physical Review Letters*, **93**, 254301.
- Wapenaar, K., D. Draganov, R. Snieder, X. Campman, and A. Verdel, 2010a, Tutorial on seismic interferometry: Part 1 — Basic principles and applications: *Geophysics*, **75**, no. 5, 75A195–75A209.
- Wapenaar, K., and J. Fokkema, 2006, Green’s function representations for seismic interferometry: *Geophysics*, **71**, no. 4, SI33–SI46.
- Wapenaar, K., E. Slob, R. Snieder, and A. Curtis, 2010b, Tutorial on seismic interferometry: Part 2 — Underlying theory and new advances: *Geophysics*, **75**, no. 5, 75A211–75A227.
- Weaver, R. L., and O. I. Lobkis, 2004, Diffuse fields in open systems and the emergence of the Green’s function: *The Journal of the Acoustical Society of America*, **116**, 2731–2734.